Supplementary material for

"How pattern formation in ring networks of excitatory and inhibitory spiking neurons depends on the input current regime"

Birgit Kriener, Moritz Helias, Stefan Rotter, Markus Diesmann, Gaute Einevoll

S1 Analysis of input current structure in the mean- and fluctuation-driven input regimes

Here, we analyze in more detail the input structure for the three input regime cases discussed in the main manuscript as well as in two further intermediate cases. Equations denoted by "Eqn. (M.n)" and figures denoted by "Fig. M.n" refer to the respective Eqn. (n) and Fig. n in the main manuscript.

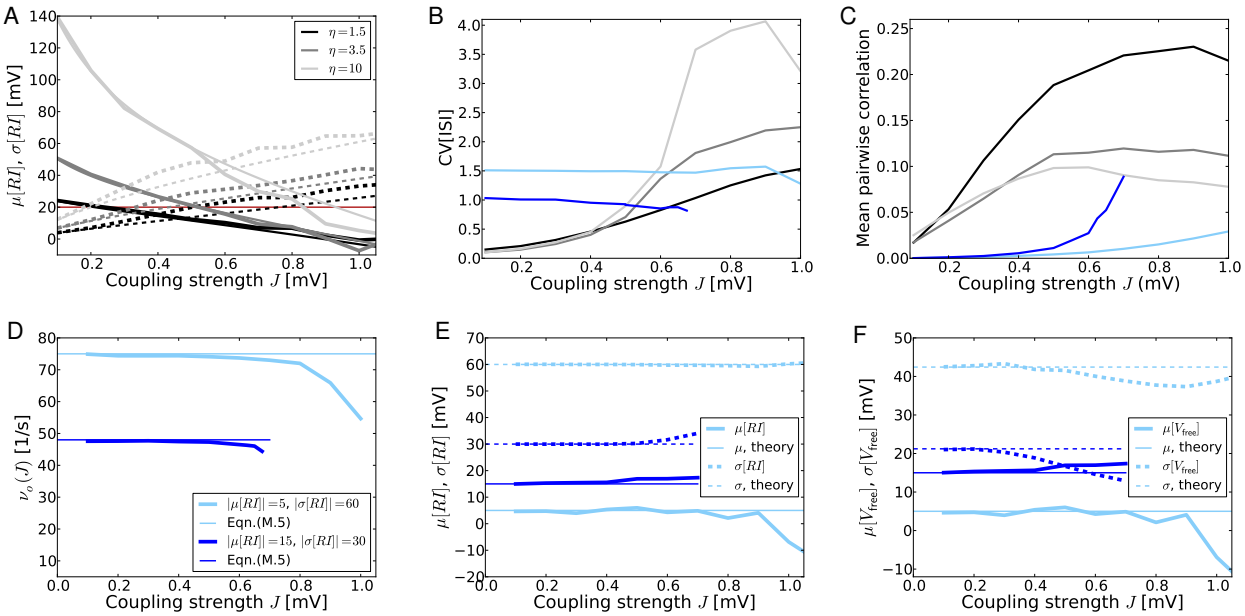

Figure 1: (A) shows the mean μ_o (solid lines) and standard deviation σ_o (dashed lines) of the total input RI as a function of J for three different values of η as predicted from Eqn. (M.5) (thin lines) in comparison to results from simulations. In all cases there is a transition from the mean-driven ($\mu > \sigma$) to the fluctuation-driven ($\sigma > \mu$) case (for orientation the horizontal red line indicates the firing threshold V_{thr}). This crossover-point shifts to the right with increasing external drive amplitude. (B) and (C) show the coefficient of variation of the interspike intervals CV[ISI] and pairwise zero-lag spike train Pearson correlation coefficient estimated from simulations (using a bin-size of $\Delta t = 0.1\,\mathrm{ms}$), respectively. The color code is the same as in panel (A). In addition we show CV and correlations in the strongly fluctuation-driven regime ($\mu[RI] = 5\,\mathrm{mV}$, $\sigma[RI] = 60\,\mathrm{mV}$ as used in Fig. M.1 D–F in light blue, and a second choice $\mu[RI] = 15\,\mathrm{mV}$, $\sigma[RI] = 30\,\mathrm{mV}$, cf. Fig. 2 C,D, in blue). (D) shows the self-consistent rate for the same two choices as predicted by Eqn. (M.5) (thin lines) versus what is obtained in simulations (thick lines). (E) depicts the mean (solid lines) and standard deviation (dashed lines) of the input RI and (F) of the free membrane potential V_{free}, respectively, measured from simulations (thick lines) in comparison to the expected values assuming uncorrelated Poisson input spike trains (thin lines). In all cases $N = 2500$, $\kappa = 0.1N$, $g = 6$, and $\beta = 0.8$.

Fig. 1 A shows mean $\mu[RI]$ (solid lines) and standard deviation $\sigma[RI]$ (dashed) of the total input as a function of coupling strength J for three different values of η ($\eta = \{1.5, 3.5, 10\}$ from black to light gray) as predicted from Eqn. (M.5) and as estimated from simulations (thicker lines). In all cases at one point the neurons change from a mean-driven ($\mu > \sigma$) to a fluctuation-driven ($\sigma > \mu$) regime. As to be expected, the smaller η is, and thus the larger the relative contribution of the net inhibitory recurrent input RI_{s},

the smaller is the coupling strength at which this switch occurs (see black curves, for orientation the red vertical line denotes the threshold V_{thr}). The mean of the input current is always well-predicted by Eqn. (M.5) for subcritical J, however the standard deviation of the input RI as observed in simulations is larger than expected by theory, independent of J (here, we simulated for 10 s per trial and averaged over ten trials per parameter tuple). The reason is the clustered, locally synchronized spiking activity in networks driven by constant external input that renders input spike trains more regular and correlated than expected for uncorrelated Poisson spike trains [1].

In Figs. 1 B and C we hence show the average coefficient of variation (CV) of interspike intervals (ISI), and the pairwise spike correlations as a function of J for the same η-values as in Fig. 1 A (same color code). The average CV[ISI] is defined by

$$\mathrm{CV[ISI]} = \frac{1}{M} \sum_{i=1}^{M} \frac{\sigma[\mathrm{ISI}_i]}{\mu[\mathrm{ISI}_i]} \,. \tag{1}$$

Again, we averaged over ten trials per parameter tuple, and for each network randomly picked $M = 500$ neurons. If spike trains have Poisson statistic, we expect a CV of one, while smaller CV indicates more regular, higher CV more irregular spiking. Indeed, Fig. 1 B shows that spiking is very regular for small coupling strength independent of η, while it increases to values higher than one around the onset of pattern formation, that occurred between $J_c = 0.5$ and 0.6 mV in the simulations. The increase is more pronounced for larger η (lighter gray levels).

The average pairwise spike train correlations as a function of J and η shown in Fig. 1 C were estimated as follows: We chose 250 adjacent neurons ($N = 2500$), i.e., a local neighborhood κ, binned the spike trains with bin width $\Delta t = 0.1$ ms and computed all pairwise zero-timelag correlation coefficients that were then averaged (cf. [1]). Spike train correlations are significant, and more so for larger J and smaller external noise amplitude η (same color code as in Fig. 1 A).

In ring networks neighboring neurons sample from basically identical input pools in the recurrent network. This leads to strong input current correlations in the case where the additional uncorrelated external Poisson noise is weak, explaining the increase with recurrent coupling strength, and decrease with external input amplitude η [1].

So we conclude that there are indeed pronounced deviations from Poisson towards more regular and synchronous activity for subcritical J that corresponds to a more mean-driven input current regime as expected by the noiseless approximation Eqn. (M.10), and hence the predictions J_c^{md} derived in this regime are appropriate.

In the following we compare these findings with the firing rate and input statistics in the strongly fluctuation-driven regime, where there is both excitatory and inhibitory external drive, adjusted such that the total input current mean and variance is the same for all J. The blue curves in Figs. 1 B and C show CV and correlations for this input regime. The light blue curves denote the choice we used in Figs. M.1 D–F, i.e., $\mu[RI] = 5$ mV and $\sigma[RI] = 60$ mV, while blue shows another choice with smaller total input variance, i.e., $\mu[RI] = 15$ mV, $\sigma[RI] = 30$ mV. In the latter case, the CV[ISI] stays at approximately one with varying J ($J = 0.7$ mV is the maximal coupling strength such that Eqn. (M.4c) stays non-negative), while in the first case the CV indicates that spiking is more irregular than expected for Poisson spiking for all values of J. This is a consequence of the high variance of the input current and resulting membrane

potential fluctuations: In effect, each neuron will spend long times at quite hyperpolarized values, corresponding to extended periods of silence, while during occasional large depolarizing input transients it can emit several spikes in a short interval. This yields more irregular output spiking than expected for a Poisson process, even for isolated neurons receiving uncorrelated Poisson input currents of such high variance (not shown)[1].
Only when these networks undergo pattern formation do we see a change to slightly smaller values that are explained by the more oscillatory activity in the emerging activity bumps (see Fig. M.1 F). For $\mu[RI] = 5\,\mathrm{mV}$ and $\sigma[RI] = 60\,\mathrm{mV}$ (light blue) pattern formation onset agrees well with the prediction by Eqn. (M.9), i.e., $J_c^{\mathrm{fd}} = 0.9\,\mathrm{mV}$, see also Fig. M.1 D–F. For $\mu[RI] = 15\,\mathrm{mV}$, $\sigma[RI] = 30\,\mathrm{mV}$ (blue), however, pattern formation occurs earlier at around $J_c \approx 0.615\,\mathrm{mV}$ versus the prediction $J_c^{\mathrm{fd}} = 0.844\,\mathrm{mV}$ (cf. also Fig. 2 C,D), although the network is clearly and by construction in the fluctuation-driven regime.

The average zero-timelag spike train correlations are shown in Fig. 1 C. They are generally low, much lower than in the constant external drive case. This is due to the weak influence of incoming spikes from the recurrent network in the highly fluctuating barrage of externally injected spikes, especially at small J. For larger J-values spike train correlations increase with the growing impact of the correlated recurrent input spike trains. As to be expected, this effect is stronger in the case of weaker noise $\mu[RI] = 15\,\mathrm{mV}$, $\sigma[RI] = 30\,\mathrm{mV}$ (blue). So also in this input regime deviations of the spiking statistics from uncorrelated Poisson may lead to deviations from the prediction of Eqn. (M.9). for the onset of pattern formation.

To investigate this further, Fig. 1 shows the self-consistent firing rates (Fig. 1 D), and mean and variance of the total input (Figs. 1 E), as well as the free membrane potential, i.e., the membrane filtered input current (Fig. 1 F). Fig. 1 D demonstrates that for both choices of mean and standard deviation of total input current, firing rates stay close to the Siegert prediction Eqn. (M.5) and only deviate to smaller values with onset of pattern formation. Still, when injecting adapted external currents via the rates Eqns. (M.4) we implicitly assume that not only the external currents are uncorrelated Poisson (which they are by construction), but also that the recurrent contributions in RI_{s} are.

To check how well mean and standard deviation of the total input current RI really adhere to the prescribed values, Fig. 1 E shows $\mu[RI]$ and $\sigma[RI]$ measured from actual simulations for varying J (thick solid and dashed line, respectively) in comparison to the expected values (thin lines). For the strongly fluctuation-driven network there is good agreement between measurement and expectation (light blue), while there are small deviations to higher mean and standard deviation for $\mu[RI] = 15\,\mathrm{mV}$, $\sigma[RI] = 30\,\mathrm{mV}$ (blue) that coincide with the increase in spike train correlations and are thus explained by them.

However, as apparent from Fig. 1 F, the free membrane potential, i.e., the membrane filtered input spike trains, shows much clearer deviations for both choices of $\mu[RI], \sigma[RI]$ from the expectation for uncorrelated Poisson input spike trains, i.e., $\mu[V_{\mathrm{free}}] = \mu[RI]$ and $\sigma[V_{\mathrm{free}}] = \sigma[RI]/\sqrt{2}$ [2]. For small J there is still good agreement, while for larger $J \gtrsim 0.5$ the standard deviations start to decrease, especially for $\mu[RI] = 15\,\mathrm{mV}$, $\sigma[RI] = 30\,\mathrm{mV}$. Hence, even if the input currents appear to agree with the assumptions underlying Eqn. (M.5), the linear filtering by the membrane reveals deviations from Poisson spiking.

To summarize Fig. 1, we note that there are clear deviations from Poisson input statistics in the regime of constant external drive (Fig. 1 A–C) that become more pronounced for larger external drive amplitude η. In this regime neurons operate in a more mean-driven regime explaining the better prediction of onset of pattern formation J_c^{md} by the noiseless approximation Eqn. (M.13).
For the constant total input current regime, that ensures that the system is in the fluctuation-

[1]We note that the Fano factor of spike counts, $F_{\Delta t} = \sigma^2[\mathrm{counts}/\Delta t]/\mu[\mathrm{counts}/\Delta t]$ has the same behavior as the CV[ISI], and is equal or larger than unity in this input regime.

driven regime for all J, the prediction J_c^{fd} by Eqn. (M.9) seems to be more appropriate if $\sigma[RI] \gg \theta$, however also here we observe input statistics that deviates from the expectation for Poisson spiking (Fig. 1 E, F).

Fig. 2 shows variance and kurtosis of the rate distribution for two other input realizations that are characterized by weak average external drive, and spiking can thus be considered fluctuation-driven. In Figs. 2 A,B the external drive is constant at $\eta = 1.5$ corresponding to a $\mu[RI] < V_{\mathrm{thr}}$ for $J > 0.2\,\mathrm{mV}$, see Fig. 1 A (black lines). The linear response-derived stability analysis Eqn. (M.9) predicts a $J_c^{\mathrm{fd}} = 3.98\,\mathrm{mV}$ ($J_c^{\mathrm{fd}|d\nu/d\mu} = 1.52\,\mathrm{mV}$), while true onset of pattern formation as observed in simulations agrees very well with the prediction by the noiseless approximation Eqn. (M.13), marked by the red dashed line in Figs. 2 A,B.

Figs. 2 C,D show variance and kurtosis, respectively, of the rate distribution for a ring network driven with external input adapted to yield constant total input with varying J, here, $\mu[RI] = 15\,\mathrm{mV}$ and $\sigma[RI] = 30\,\mathrm{mV}$. As discussed before, Eqn. (M.9) predicts a $J_c^{\mathrm{fd}} = 0.844\,\mathrm{mV}$, while true onset of pattern formation, as indicated by a sudden increase in variance and decrease in kurtosis, clearly occurs much earlier at $J_c \approx 0.615\,\mathrm{mV}$, presumably because of the deviations from the assumptions underlying Eqn. (M.5), as discussed earlier.

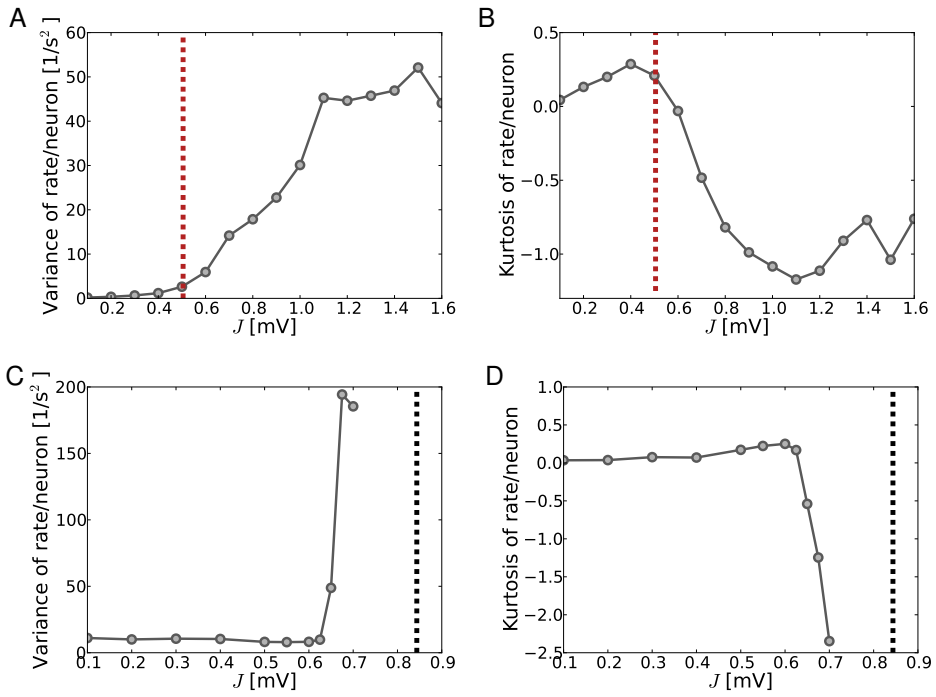

Figure 2: (A), (C) show the variance, (B), (D) the kurtosis of the rate distribution estimated from ten network simulations for two further intermediate input cases. In (A) and (B) the external input was constant with amplitude $\eta = 1.5$. Pattern formation onset occurs around $J \gtrsim J_c^{\mathrm{md}} = 0.506\,\mathrm{mV}$, similar as for $\eta = 3.5$, cf. M.5 (H,I), while Eqn. (M.9) predicts a $J_c^{\mathrm{fd}} = 3.98\,\mathrm{mV}$. In (C) and (D) external input was adjusted to ensure constant total input mean $\mu[RI] = 15\,\mathrm{mV}$ and standard deviation $\sigma[RI] = 30\,\mathrm{mV}$. Eqn. (M.9) predicts a $J_c^{\mathrm{fd}} = 0.844\,\mathrm{mV}$, while pattern formation already occurs at lower $J_c \approx 0.615$ in simulations.

Excess synchrony of the excitatory subpopulation

In this subsection we take a closer look at the individual spike statistics of the excitatory and inhibitory subpopulations in the ring.

The theory based on the linear response approximation assumes asynchronous-irregular input spike trains (Poisson-type spiking). Nearby neurons in ring networks typically have a high amount of common input that induces non-trivial pairwise correlations of output spike trains, visible as locally synchronous spike clusters. To assess the amount of excess synchrony with respect to the underlying Poisson assumption we measure the autocovariances of the compound input spike count per time interval Δt, i.e., $Z_i(t|\Delta t) = \sum_{j\in \mathrm{Pre}[i]} z_j(t|\Delta t)$, where z_j are the individual contributions of presynaptic neurons j, in relation to what is expected for a Poisson process. The resulting *relative autocovariance function of counts* $\bar{A}(\tau)$ is given by

$$\bar{A}(\tau) = \frac{\mathrm{E}[Z_i(t|\Delta t) Z_i(t+\tau|\Delta t)]}{\mathrm{E}_t[Z_i(t|\Delta)]} \tag{2}$$

$\bar{A}(0)$ is a measure that integrates the underlying autocovariance function around zero time lag [3]. If all contributing spike trains are uncorrelated Poisson processes, $\bar{A}(0) = 1$, while excess synchrony within a chosen Δt yields $\bar{A}(0) > 1$. If the autocovariance function has negative contributions, $\bar{A}(0)$ can also be smaller than unity.

Separating $Z_i(t|\Delta t)$ into the respective contributions of the excitatory and inhibitory presynaptic subpopulations, i.e., $Z_{j\in\mathrm{E}}$ and $Z_{j\in\mathrm{I}}$, reveals that the resulting inhibitory relative autocovariance $\bar{A}_\mathrm{I}(\tau)$ is lower than the excitatory one $\bar{A}_\mathrm{E}(\tau)$, even for small coupling strength J, cf. Fig. 3, in particular for larger Δt (Fig. 3 B,C). In part this is explained by the larger spatial

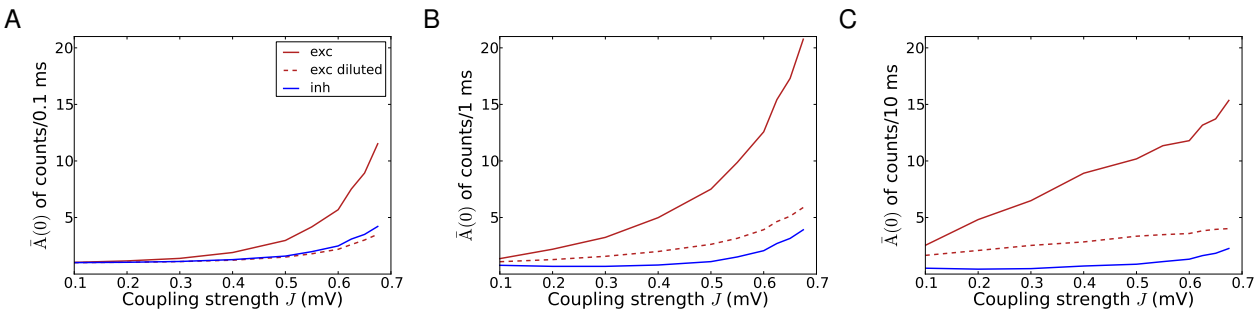

Figure 3: The zero time-lag relative autocovariances of the local excitatory (red) and inhibitory (blue) input pool for three choices of Δt (A: $\Delta t = 0.1\,\mathrm{ms}$, B: $\Delta t = 1\,\mathrm{ms}$, and C: $\Delta t = 10\,\mathrm{ms}$). The dashed red line corresponds to an excitatory population sampled at identical spatial dilution as the inhibitory one. The central peak of $\bar{A}_\mathrm{E}(\tau)$ grows with the temporal integration window Δt, whereas the peak of $\bar{A}_\mathrm{I}(\tau)$ decreases. The input scenario is the constant total input mean and variance case, with external noise (excluded from measure A) adjusted such that $\mu[RI] = 15\,\mathrm{mV}$ and $\sigma[RI] = 30\,\mathrm{mV}$. Other parameters: $N = 2500$, $\kappa = 250$, $g = 6$, $J = 0.5\,\mathrm{mV}$.

dilution of the inhibitory neurons contributing to the neuronal input: they are five neurons apart, thus any two consecutive inhibitory neurons share less common input than consecutive excitatory neurons. To correct for this we compute $\bar{A}_\mathrm{E}(\tau)$ across an equally spatially diluted sample of excitatory neurons (dashed red line in Figs. 3 A-C). For $\Delta t = 0.1\,\mathrm{ms}$ this yields comparable $\bar{A}_\mathrm{E}(\tau)$ and $\bar{A}_\mathrm{I}(\tau)$ (Fig. 3 A), while for larger Δt even the diluted sample indicates higher excess synchrony (Figs. 3 B,C).

The origin of this becomes clear when we inspect the full relative autocovariance functions, cf. Fig. 4. For small Δt, $\bar{A}_\mathrm{E}(\tau)$ is positive for all τ with approximately exponentially decaying flanks around zero time-lag. With increasing Δt more of this positive covariance is integrated into the central peak, indicating excess synchrony within Δt precision. On the other hand, $\bar{A}_\mathrm{I}(\tau)$ has negative flanks around zero time-lag, indicating a lack of near synchrony. Increasing Δt to 10 ms can thus even yield $\bar{A}_\mathrm{I}(0) < 1$.

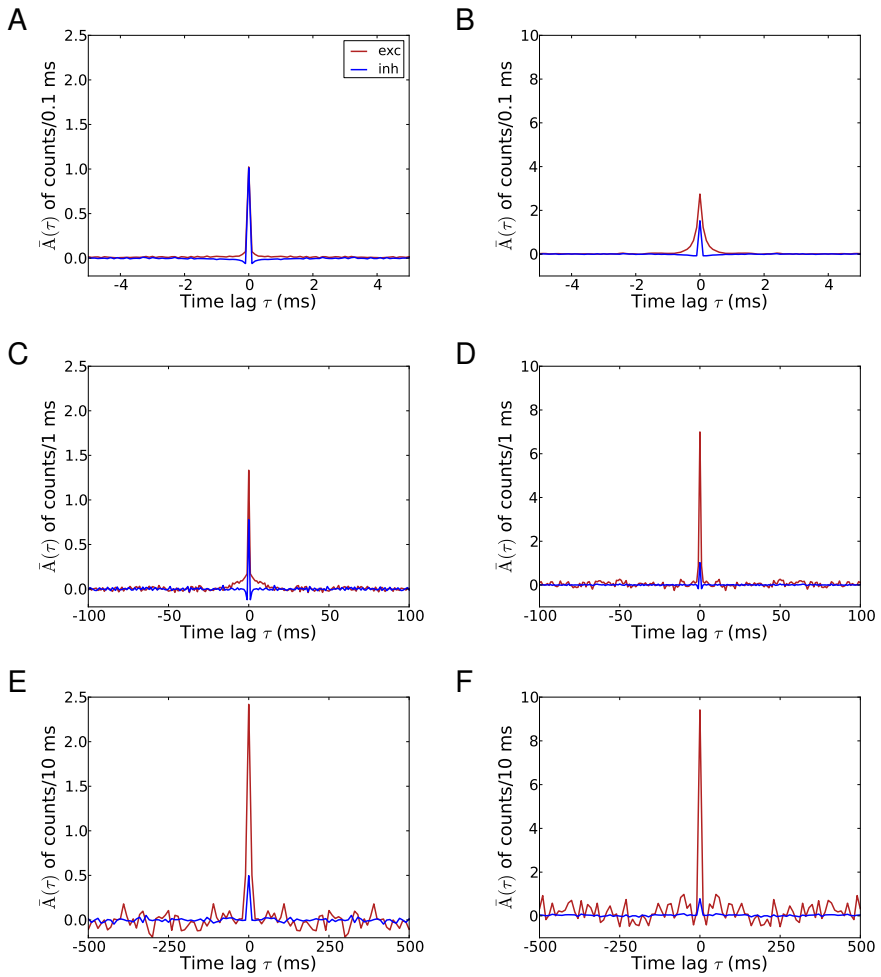

Figure 4: Full relative autocovariance functions of the excitatory (red) and inhibitory (blue) subpopulation for three different Δt ((A,B): $\Delta t = 0.1\,\mathrm{ms}$, (C,D) $\Delta t = 1\,\mathrm{ms}$, and (E,F) $\Delta t = 10\,\mathrm{ms}$). In the left column J was set to $0.1\,\mathrm{mV}$, in the right column to $0.5\,\mathrm{mV}$. Parameters as in Fig. 3.

At first sight it seems counterintuitive that excitatory and inhibitory neurons have this differing spike train statistics, because they receive the same number of excitatory and inhibitory inputs at approximately identical firing rates. The explanation for this effect lies in the local connectivity of ring networks: excess synchrony of the excitatory population will reinforce further spikes in the vicinity, while spikes from the inhibitory population decreases the instantaneous firing probability. Near synchrony is thereby effectively enhanced in the excitatory population and suppressed in the inhibitory one (also see [4] for a related discussion of this effect in the framework of balanced random networks). Such volleys of excitatory input spikes act like compound pulses with large amplitude (on the order of up to θ) in an otherwise balanced asynchronous background activity. At these amplitudes the effective gain Eqn. (M.7) derived from linear response theory becomes linear in J with a slope proportional to $1/\theta$, i.e., the slope of the linear model Eqn. (M.13). Fig. 5 demonstrates this effect. This explains the fact that Eqn. (M.13) has better predictive power also in the intermediate or weakly fluctuation-driven scenarios.

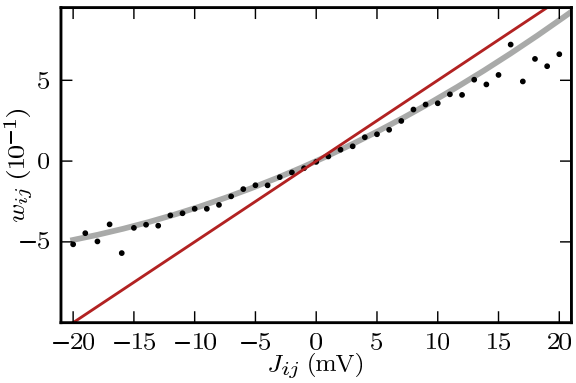

Figure 5: Effective gain $\tilde{W}$ (cf. (M.7)) as a function of network coupling strength J (gray curve) in comparison to the integrated impulse response in simulations (black dots, here $\mu[RI] = 15\,\mathrm{mV}$, $\sigma[RI] = 30\,\mathrm{mV}$) and the linear approximation (M.11) of the Siegert equation (M.5) in the noiseless limit (red line). The effective gain estimated from simulations follows the response theory predictions up to amplitudes up to $\sim 15\,\mathrm{mV}$. This is a direct consequence of the high variance of the input against which even large pulses appear comparably weak. Moreover, for high pulse amplitude J, $\tilde{W}(J)$ becomes parallel to the low-noise approximation $\tilde{W} = J/\theta$ (cf. Eqn. (M.11)).

S2 Relation of the coarse-grained model to Ermentrout-Cowan networks

In neural field modeling ring models are amongst the best-studied systems [5, 6, 7]. Neural field models are in principle derived from spiking neuron network dynamics by performing a continuum limit that yields neuron densities and spatial coupling kernels. In a common framework [9, 10, 5] the firing rate of a neuron k is given by a current $I_k(t)$ that non-linearily depends on the membrane potential by a transfer function $S(V_k(t))$, which is commonly assumed to be, e.g., a step function, a rectified linear function or a sigmoidal with activation threshold u. The input currents that arrive at a postsynaptic neuron i are then weighted, summed up and filtered by a temporal kernel $h(t)$ to give the membrane potential of the neuron, such that

$$V_i(t) = \int_{-\infty}^{t} h(t-\tau) \sum_k \alpha_{ik} S(V_k(\tau))\, d\tau + \int_{-\infty}^{t} h(t-\tau) P_i(\tau)\, d\tau\,, \tag{3}$$

where α_{ik} is the distance-dependent synaptic weight and $P(t)$ is an external current. If $h(t) = \exp[-t/\xi]/\xi$, the dynamics (3) can be transferred to a differential equation that is structurally equivalent to Eqn. (1) in the main manuscript, i.e.,

$$\xi \frac{dV_i(t)}{dt} = -V_i(t) + \sum_k \alpha_{ik} S(V_k(t)) + P_i(t)\,. \tag{4}$$

With $\alpha_{ik} = \alpha w(|i-k|)$, $\sum_k w(|k|) = 1$ the continuum limit then leads to the coupled field equations

$$\xi_{\mathcal{X}} \frac{dV_{\mathcal{X}}(x,t)}{dt} = -V_{\mathcal{X}}(x,t) + \sum_{\mathcal{Y}\in\{\mathcal{E},\mathcal{I}\}} \alpha_{\mathcal{X}\mathcal{Y}} \int_{-\infty}^{\infty} W_{\mathcal{X}\mathcal{Y}}(|x-x'|) S(V(x',t))\, dx' + P_{\mathcal{X}}(x,t)\,,\quad \mathcal{X},\mathcal{Y} \in \{\mathcal{E},\mathcal{I}\}\,. \tag{5}$$

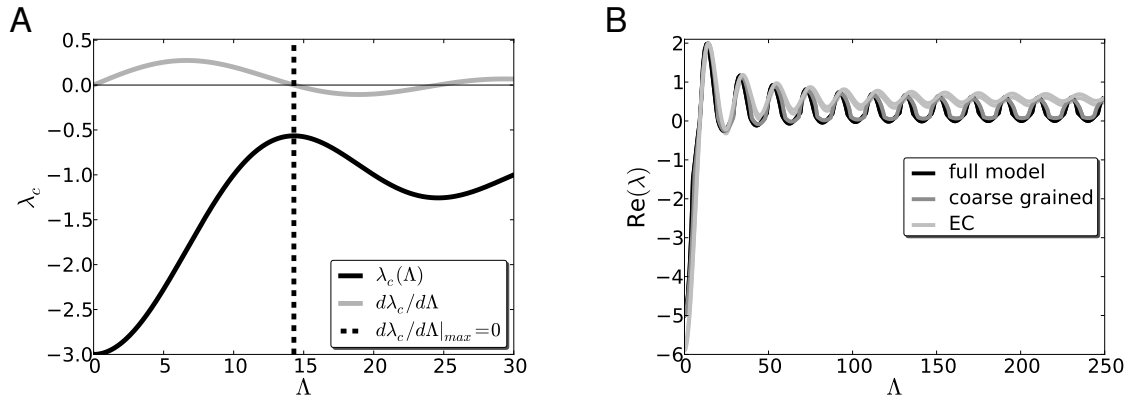

Figure 6: (A) The dispersion relation $\lambda_c(\Lambda)$ for the Ermentrout-Cowan (EC) model (black) and its derivative (gray) whose first zero gives the wavenumber of the global maximum. (B) The full model (black), the coarse-grained model (dark gray) and the EC model (light gray, here, S' was scaled to match the other two in maximal amplitude) in comparison.

for two populations $\mathcal{E}$ (excitatory) and $\mathcal{I}$ (inhibitory). Stability analysis [5] leads to a linearized dynamical system and the eigenvalues $\lambda_H(\Lambda)$ of the matrix

$$H(\Lambda) = \begin{pmatrix} S'_{\mathcal{E}}(u)\alpha_{\mathcal{E}\mathcal{E}}\hat{w}(\Lambda) - 1 & S'_{\mathcal{E}}(u)\alpha_{\mathcal{E}\mathcal{I}}\hat{w}(\Lambda) \\ S'_{\mathcal{I}}(u)\alpha_{\mathcal{I}\mathcal{E}}\hat{w}(\Lambda) & S'_{\mathcal{I}}(u)\alpha_{\mathcal{I}\mathcal{I}}\hat{w}(\Lambda) - 1 \end{pmatrix}, \tag{6}$$

– where $\hat{w}(\Lambda)$ denotes the Fourier transform of the coupling kernel – determines the stability of the spatially homogeneous mode (trivial solution) to spatially inhomogeneous perturbations of activity. In particular, for a boxcar coupling kernel $B(x, \sigma) := \Theta(|x| - \sigma)/2\sigma$ the Fourier transform is given by $\mathrm{sinc}(\sigma\Lambda) = \sin(\sigma\Lambda)/(\sigma\Lambda)$. If we assume that the transfer function is the same for all neurons, that $\alpha_{\mathcal{E}\mathcal{E}} = \alpha_{\mathcal{I}\mathcal{E}} = 4\alpha$, and $\alpha_{\mathcal{E}\mathcal{I}} = \alpha_{\mathcal{I}\mathcal{I}} = -g\alpha$, and moreover substitute $S'(u) =: s'$, we obtain

$$H(\Lambda) = \begin{pmatrix} 4s'\alpha\,\mathrm{sinc}(\sigma\Lambda) - 1 & -gs'\alpha\,\mathrm{sinc}(\sigma\Lambda) \\ 4s'\alpha\,\mathrm{sinc}(\sigma\Lambda) & -gs'\alpha\,\mathrm{sinc}(\sigma\Lambda) - 1 \end{pmatrix}. \tag{7}$$

With spatial extent $\sigma = 2\pi\kappa/N$ of the coupling kernel on two rings of circumference 2π and neuron densities $N_\mathrm{I}/2\pi$ and $N_\mathrm{E}/2\pi = 2N_\mathrm{I}/\pi$, respectively, we can thus map the ring model discussed previously to the neural field model of [5]. The resulting eigenvalues are $\lambda_H(\Lambda) = \{-1, -1 - 2\mathrm{sinc}(\sigma\Lambda)\}$, where $\mathrm{sinc}(x) = \sin(\pi x)/\pi x$. The latter eigenvalue $\lambda_c(\Lambda)$ gives the dispersion relation $f(\Lambda)$ whose maximum determines which wavenumber will grow after a spatial perturbation and is scaled and plotted in comparison to the respective relations from Secs. 3.2 and 3.4 in the main manuscript in Fig. 6 B. The maximum can be determined by finding the zero of the derivative of λ_c with respect to Λ, and is close to but not exactly an integer number (here ≈ 14.3, cf. Fig. 6 A), such that a rounding operation is needed to obtain the Fourier mode $v_c \sim e^{i\Lambda x}$ that complies with the constraint of periodic boundary conditions.

We note that to relate the coarse-grained model to the classical result of Ermentrout and Cowan (1980), we specify the non-linearity in the latter work only up to the point that the derivative S' matches the linearized gain of the coarse-grained model in Fig. 6 A.

S3 Comparison to two-dimensional torus-grids

Analogous to the way of computing the eigensystem in the one-dimensional case the eigensystem of a two-dimensional torus-grid can be computed in the following way.

The nodes of the network are distributed on a regular 2-dimensional grid with edge length N, such that $N \bmod 2 = 0$. We assume that each fourth neuron is inhibitory as indicated in Fig. 7 A the gray dots mark the inhibitory, black ones the excitatory neurons, the boundary conditions are assumed to be periodic. The κ nearest neurons of a neuron i shall be neighbors of i with respect to the l^∞-norm, such that $\kappa = 4K(K+1)$, where K is the number of the quadratic shells surrounding each node. If we want $\kappa/N^2 \approx \epsilon \in [0,1]$, $K = \lfloor \frac{1}{2}\sqrt{1+\epsilon N^2} - \frac{1}{2} \rfloor$.

We will now solve the eigenvalue problem for the general case of a unit cell of size $M \times M$ with $M \leq N$ and $N \bmod M = 0$. The grid indices $\{i,j\},\ i,j = \{0,...,N-1\}$ map to the node indices n by

$$n = Ni + j,\ n \in \{0,...,N^2-1\},\ i = \left\lfloor \frac{n}{N} \right\rfloor,\ j = n \bmod N\,. \tag{8}$$

In grid indices we see that there are two invariant translation operations

$$T_i : \{i,j\} \to \{(i+M) \bmod N, j\} \tag{9}$$

and

$$T_j : \{i,j\} \to \{i, (j+M) \bmod N\}\,. \tag{10}$$

Hence,

$$T_i[n] = N\ \left[\left(\left\lfloor \frac{n}{N} \right\rfloor + M \right) \bmod N \right] + n \bmod N \tag{11}$$

$$T_j[n] = N\ \left\lfloor \frac{n}{N} \right\rfloor + (n+M) \bmod N \tag{12}$$

The arbitrary translation about p cells in i- and q cells in j-direction across the grid is given by

$$T_i^p\, T_j^q\, [n] = N \left[\left(\left\lfloor \frac{n}{N} \right\rfloor + p\, M \right) \bmod N \right] + (n + q\, M) \bmod N\,. \tag{13}$$

We see that due to the symmetry properties of the system the coupling matrix W and the shifting operator $T_{p\,q} = T_i^p T_j^q$ commute, i.e., $[T_{p\,q}, W] = 0$ and so we can diagonalize both operators in a common basis of eigenvectors. The translation operators are unitary operators and thus have eigenvalues φ_l, ϑ_k and eigenvectors w_l, v_k, such that

$$\begin{aligned} T_i\, w_l &= e^{i\alpha_l}\, w_l = \varphi_l\, w_l\,, \\ T_j\, v_k &= e^{i\beta_k}\, v_k = \vartheta_k\, v_k\,. \end{aligned} \tag{14}$$

Due to the periodic boundary conditions the eigenvalues must fullfil

$$\begin{aligned} T_i^{N/M}\, w_l &= w_l \ \Rightarrow\ \alpha_l = 2\pi l M/N,\ l \in \{0,...,N/M-1\}\,, \\ T_j^{N/M}\, v_k &= v_k \ \Rightarrow\ \beta_k = 2\pi k M/N,\ k \in \{0,...,N/M-1\}\,. \end{aligned} \tag{15}$$

In our notation Eqn. 8, the node indices of the unit cell indices $m \in \{0,...,M^2-1\}$ of the nodes marked by the red rectangle in Fig. 7 A (we start counting in the lower left corner and go on from left to right and finish in the upper right corner) are mapped to the global node index as $n = \iota(m)$, with

$$\iota\ :\ \{0,...,M^2-1\} \to \{0,...,N^2-1\},\quad m \mapsto m \bmod M + N\ \left\lfloor \frac{m}{M} \right\rfloor\,. \tag{16}$$

Again we can define a map η from the M^2-dimensional space of the unit cell elements to the $\mathbb{C}^{M^2} \subset \mathbb{C}^{N^2}$

$$\eta \,:\, \mathbb{C}^{M^2} \to \mathbb{C}^{M^2} \subset \mathbb{C}^{N^2}, \quad \tilde{w} \mapsto w = \sum_{i=0}^{M^2-1} \tilde{w}_i \, \mathrm{e}_{\,\iota(i)} \tag{17}$$

with $\mathrm{e}_{\,i}$ the i-th canonical basis vector of the $\mathbb{R}^{N^2}$, $\tilde{w}$ the vector living on the sub-cell $M \times M$, and the operator family

$$P_{k\,l} = \sum_{p,q=0}^{N/M-1} T_{p\,q}\, e^{-i2\pi \frac{M}{N}(kp+lq)} \tag{18}$$

with $k, l \in \{0, ..., N/M-1\}$.
$(P_{k\,l} \circ \eta)$ is an isomorphism

$$(P_{k\,l} \circ \eta) : \mathbb{C}^{M^2} \subset \mathbb{C}^{N^2} \to \mathrm{Eig}(T_{p\,q}, \varphi_l, \vartheta_k)\,, \tag{19}$$

as can be readily checked again. The effective eigenvalue problem is hence given by

$$(\eta^{-1} \circ W \circ P_{k\,l} \circ \eta)\tilde{w} = \lambda_{k\,l}\tilde{w}\,. \tag{20}$$

The eigenvectors of the full matrix W are again produced by applying $P_{k\,l} \circ \eta$ to the corresponding four-dimensional eigenvector of the reduced system.

For the two-dimensional embedding the grid-layout as sketched in Fig. 7 (A) was chosen (note however, that other grid embeddings can be dealt with in the same way). With this layout there are only 75% excitatory cells in the system, hence $\beta = 0.75$. For all other parameters as before, the two-dimensional system is less stable with regard to the coupling strength J if compared to the one-dimensional system, with inhibition being more dominant. However, if scaled to the same mean input, the torus grid is in general more stable with regard to increase in J.

S4 Input-output relation is linear for large σ_o

As a heuristic observation, we note in the main manuscript, that in the large-σ_o-limit , i.e., $\sigma_o \gg \mu_o$, the integrand of Eqn. 21 becomes basically unity, and the integral thus scales as $\nu_o^{-1} \sim \sqrt{\pi}\tau_{\mathrm{m}}\theta/\sigma_o$. In particular, the input-output-relation

$$\nu_o^{-1} = \tau_{\mathrm{ref}} + \tau_{\mathrm{m}}\sqrt{\pi} \int_{\frac{V_{\mathrm{res}}-\mu_o}{\sigma_o}}^{\frac{V_{\mathrm{thr}}-\mu_o}{\sigma_o}} \exp\left[x^2\right]\,(1+\mathrm{erf}[x])\,dx, \tag{21}$$

for $V_{\mathrm{res}} = 0$ takes the following linear form in σ_o:

$$\nu_o(\sigma_o, \mu_o) = \frac{1}{\tau_{\mathrm{m}}\sqrt{\pi}}\left(\frac{\sigma_o + \mu_o}{\theta} - \frac{1}{\pi}\right)\,. \tag{22}$$

The validity of this approximation is demonstrated in Fig. 8.

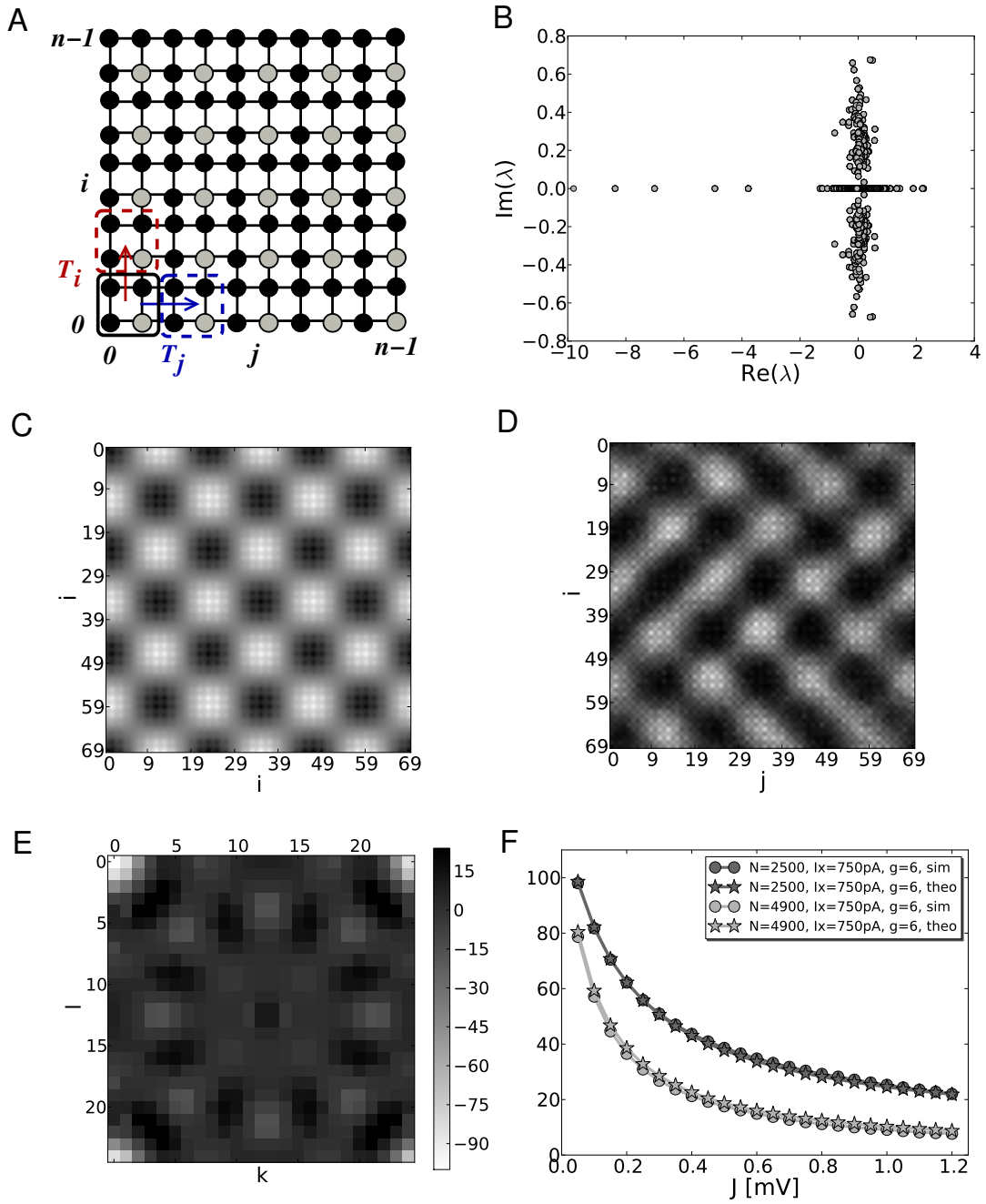

Figure 7: (A) Network layout of the torus grid network (gray dots: inhibitory, black: excitatory, red: minimal cell). (B) Eigenvalue spectrum of the rescaled coupling matrix for $N = 4900$ and $g = 6$. (C) Critical eigenvalue and (D) rate distribution in the supracritical regime. (E) shows the dispersion relation, i.e., the realpart of the eigenvalue as a function of the wavenumber. (F) shows the rate predictions from the simple linear rate model together with the simulation results.

References

[1] Kriener, B., Helias, M., Aertsen, A., and Rotter, S. (2009) Correlations in spiking neuronal networks with distance dependent connections. *Journal of Computational Neuroscience*, 27, 177–200.

[2] Amit, D. and Brunel, N. (1997) Model of global spontaneous activity and local structured activity during delay periods in the cerebral cortex. *Cerebral Cortex*, 7, 237–252.

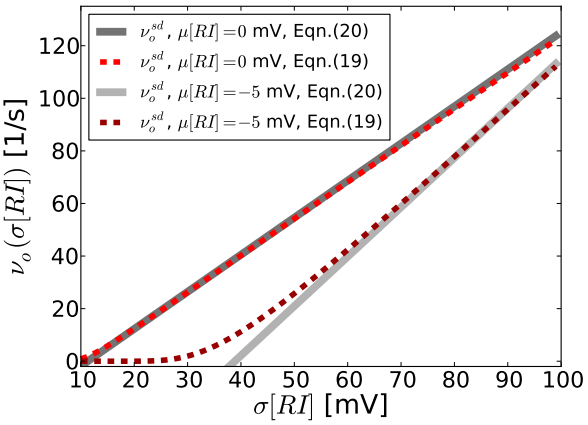

Figure 8: The figure demonstrates that the input-output-relation of the LIF neuron Eqn. 21 indeed gets linear also in the fluctuation-driven regime, cf. Eqn. 22. The gray lines show the linear predictions, while the red curves are the corresponding self-consistent rate given by Eqn. 21. Other parameters are $\theta = 20\,\mathrm{mV}$, $\tau_\mathrm{m} = 20\,\mathrm{ms}$, $\tau_\mathrm{ref} = 0.1\,\mathrm{ms}$ for $\mu = 0\,\mathrm{mV}$, while $\theta = 60\,\mathrm{mV}$, $\tau_\mathrm{m} = 5\,\mathrm{ms}$ for $\mu = -5\,\mathrm{mV}$.

[3] Tetzlaff, T., Rotter, S., Stark, E., Abeles, M., Aertsen, A. and Diesmann, M. (2008) Dependence of neuronal correlations on filter characteristics and marginal spike-train statistics. *Neural Computation*, 20(9), 2133–2184.

[4] Helias, M., Tetzlaff, T., and Diesmann, M. (2013) Echoes in correlated neural systems. *New Journal of Physics*, 15, 023002.

[5] Ermentrout, B. and Cowan, J. (1980) Large scale spatially organized activity in neural nets. *SIAM Journal for Applied Mathematics*, 38, 1–21.

[6] Ben-Yishai, R., Bar-Or, R.L., Sompolinsky, H. (1995) Theory of orientation tuning in visual cortex. *Proceedings of the National Academy of Sciences*, 92, 3844–3848.

[7] Roxin, A., Brunel, N., and Hansel, D. (2005) The role of delays in shaping spatio-temporal dynamics of neuronal activity in large networks. *Physical Review Letters*, 94, 238103.

[8] Coombes, S. (2005) Waves, bumps, and patterns in neural field theories. *Biological Cybernetics*, 93, 91–108.

[9] Ermentrout, G. B. and Cowan, J. D. (1979) A mathematical theory of visual hallucination patterns. *Biological Cybernetics*, 34, 137–150.

[10] Ermentrout, G. B. and Cowan, J. D. (1979) Temporal oscillations in neuronal nets. *Journal of Mathematical Biology*, 7, 265–280.